



HAL
open science

The horizontal dam break problem for slow non-Newtonian power-law fluids

Pierre Saramito, Claude Smutek, Benoit Cordonnier

► **To cite this version:**

Pierre Saramito, Claude Smutek, Benoit Cordonnier. The horizontal dam break problem for slow non-Newtonian power-law fluids. 2010. hal-00463791v1

HAL Id: hal-00463791

<https://hal.science/hal-00463791v1>

Preprint submitted on 15 Mar 2010 (v1), last revised 5 Sep 2013 (v4)

HAL is a multi-disciplinary open access archive for the deposit and dissemination of scientific research documents, whether they are published or not. The documents may come from teaching and research institutions in France or abroad, or from public or private research centers.

L'archive ouverte pluridisciplinaire **HAL**, est destinée au dépôt et à la diffusion de documents scientifiques de niveau recherche, publiés ou non, émanant des établissements d'enseignement et de recherche français ou étrangers, des laboratoires publics ou privés.

The horizontal dam break problem for slow non-Newtonian power-law fluids

P. Saramito^a C. Smutek^b B. Cordonnier^b

^a*LJK – CNRS et Universités de Grenoble, B.P. 53, 38041 Grenoble cedex 9, France*

^b*Laboratoire géosciences – IGP et université de La Réunion, France*

Abstract – The dam break problem shallow approximation for laminar flows of viscoplastic non-Newtonian fluids is revisited numerically with a time and space second order adaptive method. Theoretical solutions are compared both with some available measurements from the literature and with new ones on silicon. Asymptotic behaviors are studied, both numerically and as obtained from some autosimilar solutions: these theoretical results are compared with experiments. These comparisons confirm the validity of the shallow approximation equations for the horizontal dam break problem.

Keywords – viscoplastic fluid; dam break problem; shallow flows.

1. Introduction

The dam break problem in a horizontal channel is a classical problem in fluid mechanics and is motivated by numerous applications in environment and industrial processes. For a Newtonian fluid, this problem was motivated by hydraulic engineering applications. In 1887, Barré de Saint-Venant [7] introduced the shallow water approximation for fast Newtonian flows, driven by inertia terms while viscous effects are neglected. More recent studies investigated slower flows [15] and the effect of viscous terms [11]. But only the more complex non-Newtonian case can approach both for the manufacturing processes (concretes, foods) and for environmental applications, such as mud flows [9,16], volcanic lava [12], dense snow avalanches [2] and submarine landslides [13]. A shallow approximation of the dam break problem for a non-Newtonian viscoplastic fluid was first studied in 1990 by Lui and Mei [17] and revisited in 1999 by Balmforth and Craster [4]. See [6,3] for recent reviews on this subject.

Despite these numerous applications, and the development of theoretical results, few experimental measurements are available for the classical case of the horizontal dam break problem: the Newtonian case has been investigated with glucose in [20] while the non-Newtonian one is developed in [5] with a power-law and viscoplastic fluids. The purpose of this paper is to bring some new measurements in the non-Newtonian power-law case and demonstrates a new efficient numerical method for the resolution of the shallow approximation of the problem.

Email address: Pierre.Saramito@imag.fr (P. Saramito).

Section 2 presents the dam break problem statement and section 3 the reduced problem obtained after the asymptotic analysis under the shallow flow approximation. Section 4 presents the numerical results and finally, section 5 develops the experimental measurements and the comparison between theory and experiments for the presents results and previous measurements available in the literature. Appendix A develops details of the numerical resolution of this nonlinear problem.

2. Problem statement

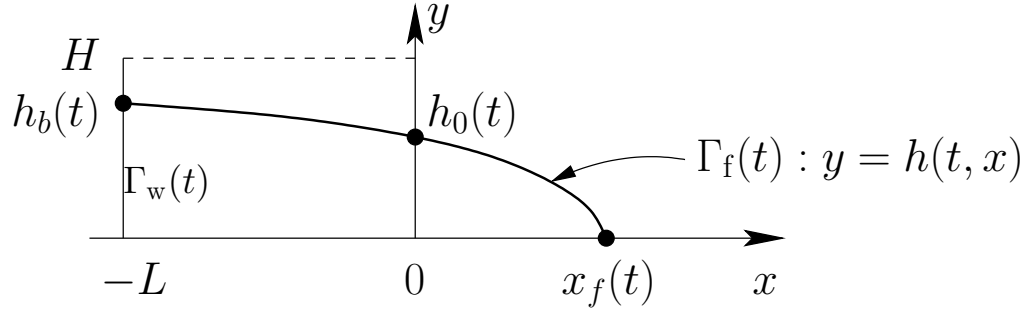


Figure 1. Schematic view of the dam break problem.

The classical bidimensional dam break problem for a power-law quasi-Newtonian fluid model is considered for leads to the following problem:

find the velocity field \mathbf{u} and the pressure field p , defined for all time $t > 0$ and in the time-dependent domain $\Omega(t)$, such that:

$$\rho \left(\frac{\partial \mathbf{u}}{\partial t} + \mathbf{u} \cdot \nabla \mathbf{u} \right) - \operatorname{div} \left(2\kappa |D(\mathbf{u})|^{n-1} D(\mathbf{u}) \right) + \nabla p = \rho \mathbf{g} \quad \text{in }]0, +\infty[\times \Omega(t), \quad (1)$$

$$\operatorname{div} \mathbf{u} = 0 \quad \text{in }]0, +\infty[\times \Omega(t), \quad (2)$$

$$\mathbf{u}(t=0) = 0 \quad \text{in } \Omega(0), \quad (3)$$

$$\mathbf{u} = 0 \quad \text{on }]0, +\infty[\times \Gamma_w(t), \quad (4)$$

$$\sigma \cdot \mathbf{n} = 0 \quad \text{on }]0, +\infty[\times \Gamma_f(t), \quad (5)$$

where ρ is the constant density, κ the constant consistency, $n > 0$ the power-law index and \mathbf{g} the gravity force vector. When $n = 1$, the fluid is Newtonian, with the classical Navier-Stokes equations. The shear thinning behavior is associated with $0 < n < 1$ and the shear thickening behavior to $n > 1$. The notation $|D(\mathbf{u})|$ denotes the second invariant of the rate of deformation tensor $D(\mathbf{u}) = (\nabla \mathbf{u} + \nabla \mathbf{u}^T)/2$. Here, (1) and (2) are respectively the momentum and mass conservation equations for an isochoric fluid. These equations are completed with the appropriate initial and boundary conditions: an initial condition for the velocity (3), adhesion at the wall of the reservoir (4), and equilibrium at the free surface (5), where surface tension is neglected. Here, $\sigma = -p.I + 2\kappa |D(\mathbf{u})|^{n-1} D(\mathbf{u})$ is the total stress tensor. The pressure outside the free surface is supposed to be constant (i.e. the atmospheric pressure). Since the pressure is defined here up to a constant, we can define by convention the atmospheric pressure as zero. The fluid domain and the free surface are respectively defined for all time $t \geq 0$ by

$$\begin{aligned}\Omega(t) &= \{(x, y) \in]-L, +\infty[\times]0, H[; \phi(t, x, y) < 0\}, \\ \Gamma_f(t) &= \{(x, y) \in]-L, +\infty[\times]0, H[; \phi(t, x, y) = 0\},\end{aligned}$$

where $\phi(t, x, y) = y - h(t, x)$ is the indicator function the flow domain and $h(t, x)$ is the flow height at time t and position x (see Fig. 1). The wall part of the flow domain boundary is simply $\Gamma_f(t) = \partial\Omega(t) - \Gamma_f(t)$.

The flow domain is transported by the velocity: $\frac{\partial\phi}{\partial t} + \mathbf{u} \cdot \nabla\phi = 0$ that writes equivalently as:

$$\frac{\partial h}{\partial t}(t, x) + u_x(t, x, h(t, x)) \frac{\partial h}{\partial x}(t, x) = u_y(t, x, h(t, x)), \quad \forall (t, x) \in]0, +\infty[\times]0; +\infty[, \quad (6)$$

where $\mathbf{u} = (u_x, u_y)$. This equation is completed with the initial condition

$$h(t=0, x) = \begin{cases} H & \text{when } -L < x < 0, \\ 0 & \text{when } x > 0. \end{cases} \quad (7)$$

3. The reduced problem

In the context of Bingham [8] fluids, Liu and Mei [17] proposed an asymptotic analysis for slow flows and small ratio H/L . Revisited in [4], this analysis has also been extended to an Herschel-Bulkley [14] fluid or a fluid with a power-law index n (see also [5]).

For a fluid with a power-law index, the height $h(t, x)$ is the single remaining unknown of the reduced problem:

(P): find h , defined in $]0, +\infty[\times]-L, +\infty[$, such that

$$\frac{\partial h}{\partial t} - \left(\frac{\rho g}{K}\right)^{\frac{1}{n}} \frac{\partial}{\partial x} \left(q_n \left(h, \frac{\partial h}{\partial x} \right) \right) = 0 \quad \text{in }]0, +\infty[\times]-L, +\infty[\quad (8)$$

$$\frac{\partial h}{\partial x}(t, -L) = \frac{\partial h}{\partial x}(t, +\infty) = 0, \quad \forall t \in]0, +\infty[\quad (9)$$

$$h(0, x) = \begin{cases} H & \text{when } x < 0 \\ 0 & \text{otherwise} \end{cases} \quad (10)$$

where, for all $\xi \geq 0$ and $\zeta \in \mathbb{R}$:

$$q_n(\xi, \zeta) = \begin{cases} 0, & \text{when } \zeta = 0, \\ \frac{n}{2n+1} \xi^{2+\frac{1}{n}} |\zeta|^{\frac{1}{n}} \text{sgn}(\zeta), & \text{otherwise} \end{cases}$$

We introduce the dimensionless quantities:

$$\hat{h} = \frac{h}{H}, \quad \hat{x} = \frac{x}{L}, \quad \hat{t} = \frac{t}{T}$$

where

$$T = \frac{L}{H} \left(\frac{KL}{\rho g H^2} \right)^{\frac{1}{n}}$$

Then, the dimensionless reduced problem writes:
 (\hat{P}): find \hat{h} , defined in $]0, +\infty[\times]-1, +\infty[$, such that

$$\frac{\partial \hat{h}}{\partial \hat{t}} - \frac{\partial}{\partial \hat{x}} \left(q_n \left(\hat{h}, \frac{\partial \hat{h}}{\partial \hat{x}} \right) \right) = 0 \quad \text{in }]0, +\infty[\times]-1, +\infty[\quad (11)$$

$$\frac{\partial \hat{h}}{\partial \hat{x}}(\hat{t}, -1) = \frac{\partial \hat{h}}{\partial \hat{x}}(\hat{t}, +\infty) = 0, \quad \forall \hat{t} \in]0, +\infty[\quad (12)$$

$$\hat{h}(0, \hat{x}) = \begin{cases} 1 & \text{when } \hat{x} < 0 \\ 0 & \text{otherwise} \end{cases} \quad (13)$$

This is a parabolic nonlinear problem, with only n as a parameter. Notice that this problem does not reduce to the usual shallow water model introduced by Barré de Saint-Venant [7] for turbulent flows: here, the viscous term is not neglected while the inertia one is eliminated during the asymptotic analysis.

4. Numerical results and comments

Here are the numerical results when $n = 1$ i.e. for a Newtonian fluid.

4.1. Position of the free surface

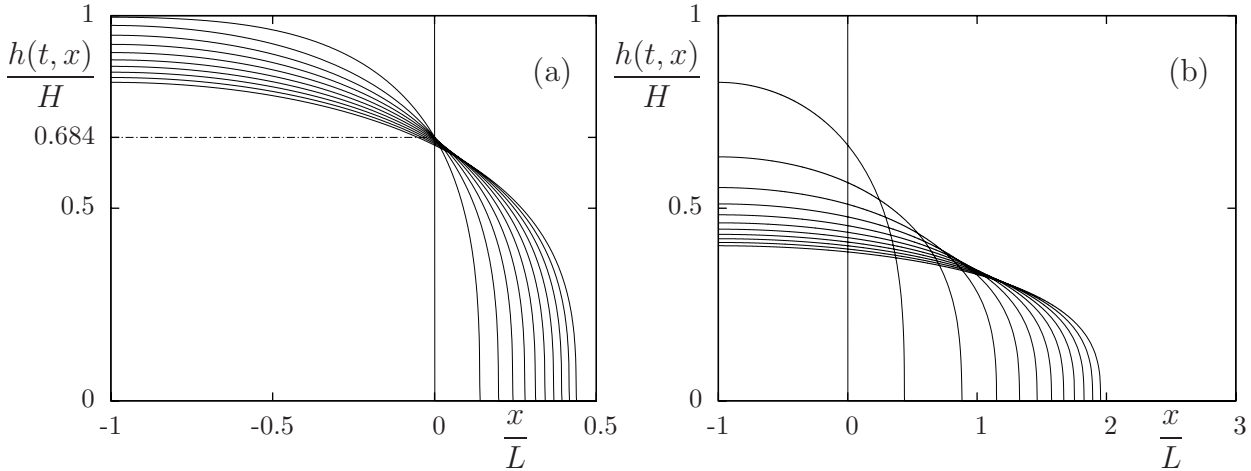


Figure 2. Evolution of the free surface for $n = 1$: (a) for small times ($t/T = 0, 0.24, 0.48, \dots, 2.4$, from left to right); (b) for medium times ($t/T = 2.4, 12, 24, \dots, 120$, from left to right).

For short times, front position and upstream level move rapidly, but at the dam position ($x = 0$) the fluid height remains constant $h(t, x=0) \approx 0.684 H$ (Fig. 2.a). For larger times, when $t > T$, the fluid height starts to decrease significantly at the dam position (Fig. 2.b), while the front position and the free surface in the reservoir move slower and the level of the free surface in the reservoir is lower and lower.

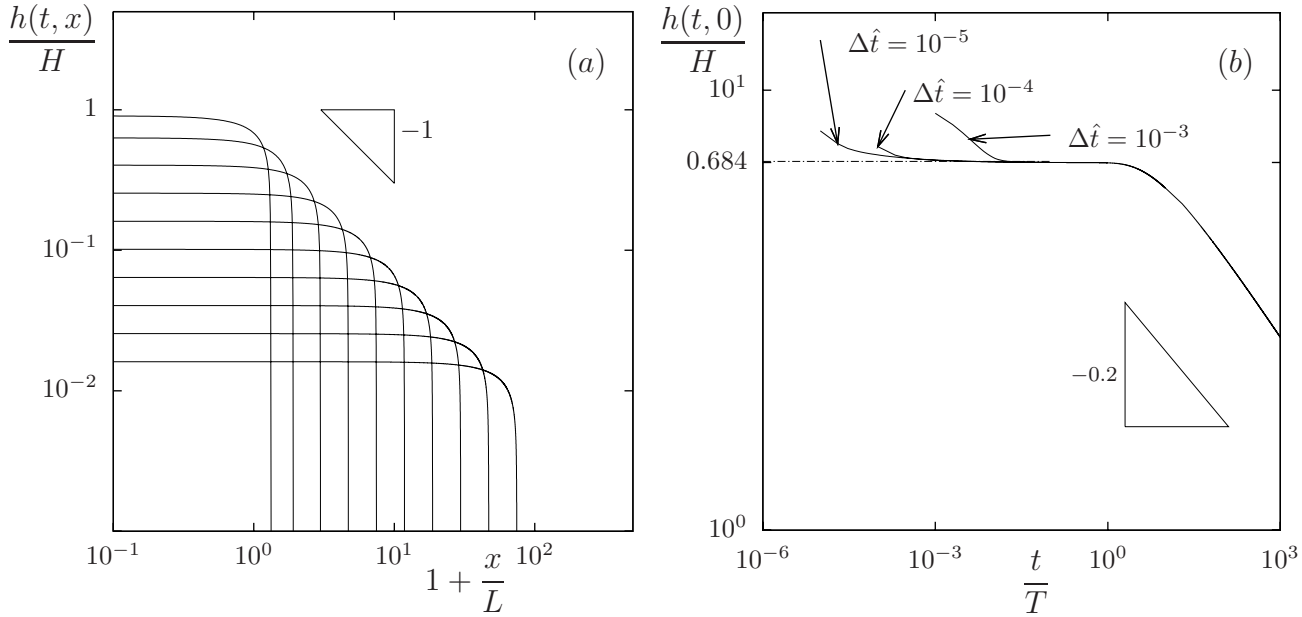


Figure 3. Evolution of the free surface when $n = 1$: (a) for large times ($t/T = 1.2, 1.2 \times 10^1, 1.2 \times 10^2, \dots, 1.2 \times 10^7$, from left to right); (b) flow height $h(t, 0)$ at the dam.

This behavior is associated with the beginning of a second flow regime. For long times (see Fig. 3.a) the envelope of free surfaces follows a $L/(L+x)$ law while the front position and the flow height in the reservoir show a power-law character. Before going further in the analysis of long-time behavior, let us study the more classical one $h(t, 0)$ for small times.

The initial condition $h(t=0, x)$ is not continuous in $x = 0$: the left value is 1 while the right value is zero. Therefore, the exact solution h is not regular for short times too. Thus, the convergence becomes difficult in the vicinity of $t = 0$. Fig. 3.b shows the convergence study for $\Delta \hat{t} = 10^{-3}, 10^{-4}$ and 10^{-5} while $\Delta \hat{x} = 10^{-4}$. The plot, in logarithmic scale, shows that the fluid height at the dam position tends to remain constant for any arbitrary short time, while the corresponding height is not defined for $(t, x) = (0, 0)$. This result suggests that convergence of $h(t, x=0)$ also occurs when t becomes small, though in a weaker sense than the usual continuous one. In practice, and for all computations in this paper, both the time steps $\Delta \hat{t}$ and element sizes $\Delta \hat{x}$ are automatically adapted, as shown in appendix A. Remark also that $h(t, x=0)$ presents a decreasing power-law behavior for long times. Fig. 3.b shows the long-time behavior. The time approximation uses a geometrical progression $t_{m+1} = \alpha t_m$ where $\alpha = 10^{0.01}$ in order to match efficiently both short and long-time asymptotic behaviors. This approximation uses 100 time steps per decade. For long times $h(t, x=0)$ behaves as $t^{-1/5}$.

4.2. The front position

Fig. 4.a shows the front position for various values of n . Observe the overall change in slope in the logarithmic scale plot. For short times, $x_f(t)$ behaves as \sqrt{t} while for long times it behaves as $t^{1/5}$. The

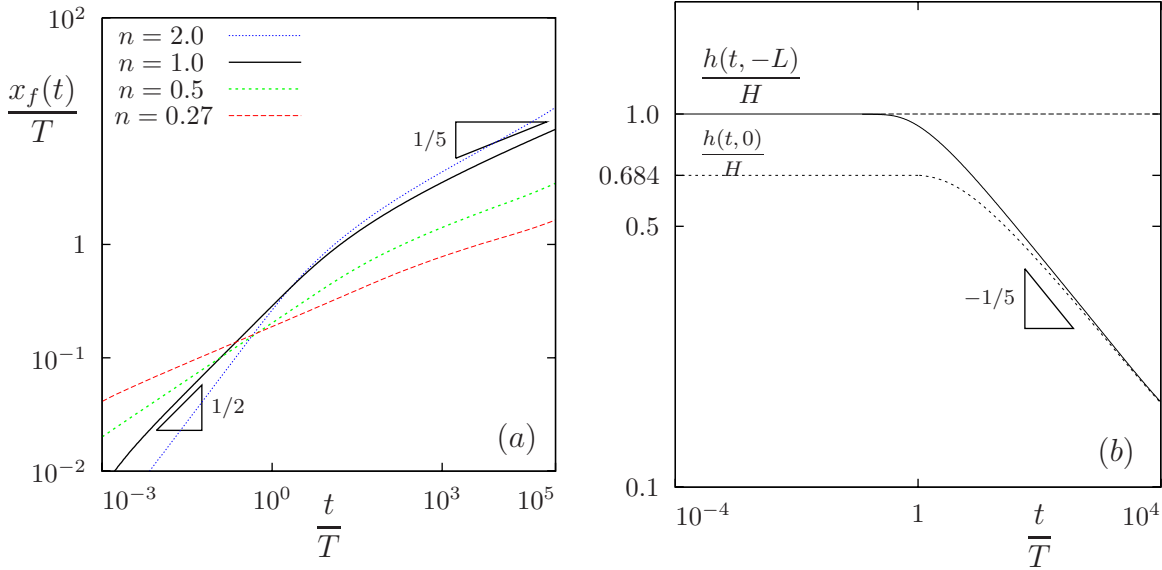


Figure 4. (a) Front position $x_f(t)$ for various n ; (b) Flow height $h(t, -L)$ in the reservoir when $n = 1$.

problem admits two similarity solutions associated to the short- and long-time behaviors [15,20,5]. This analysis suggests the following scaling law:

$$\frac{x_f(t)}{L} \approx \begin{cases} 0.284 \left(\frac{t}{T}\right)^{1/2} & \text{if } t < 2.5T \\ 1.133 \left(\frac{t}{T} + 1.221\right)^{1/5} - 1 & \text{otherwise} \end{cases} \quad (14)$$

The scaling law is not plotted here since there is no further perceptible difference on a graphical representation. More precisely, the relative error is less than 5% and the maximum is always reached in the transition regime while the relative error outside the transition regime is less than 1%. Since the purpose of the scaling law is to obtain an easy-to-use formula, (14) will be of great interest for practical applications as no more numerical computations will be required to predict the front position.

The general extension to any $n > 0$ writes:

$$\frac{x_f(t)}{L} \approx \begin{cases} a_n \left(\frac{t}{T^*}\right)^{\frac{n}{1+n}}, & \text{when } \frac{t}{T^*} < \alpha \\ b_n \left(\frac{t}{T^*} + c_n\right)^{\frac{n}{3+2n}} - 1, & \text{otherwise} \end{cases}$$

where

$$a_n = \frac{1}{3} + 0.944 \left(\frac{n}{1 + 0.548n} \right)^{0.85}, \quad b_n = \left\{ \frac{2(1+n)^{n+4}}{2+n} \left(\frac{3+2n}{n} \right)^n \beta \left(\frac{1}{1+n}, \frac{3+n}{2+n} \right)^{-2-n} \right\}^{\frac{1}{3+2n}},$$

$$c_n = \alpha - \left(\frac{1 + a_n \alpha^{\frac{n}{1+n}}}{b_n} \right)^{\frac{3+2n}{n}}, \quad T^* = \frac{1+2n}{n} (2+2n)^{\frac{1}{n}} T.$$

Constant b_n is provided by explicit formula associated to long times flow regime, while a_n is obtained numerically. Here $\beta(.,.)$ denotes the beta function. The continuity between the two flow regimes is enforced at some dimensionless transition time $t/T_* = \alpha$ by choosing an appropriate c_n , where, $\alpha = 2.5$ was used for practical comparisons with direct numerical computations.

4.3. Flow height in the reservoir

Fig. 4.b presents the computation of reservoir height $h(t, x = -1)$ at position $x = -1$ when $n = 1$. For short times, the height at the dam position and the end of the reservoir remain constants (i.e. $h(t, 0)/H = 0.684$ and $h(t, -L) = 1$) while the surface shape rearranges. For long times, $h(t, -L)$ exhibits a power law $t^{-0.2}$ behavior that matches those of $h(t, 0)$. As a result, for long times, the flow height in the reservoir becomes roughly constant versus x and decreases versus time as:

$$\frac{h(t, x)}{H} \approx 0.535 \left(\frac{t}{T} \right)^{-1/5}, \quad -L \leq x \leq 0 \text{ and } t/T_* \gg 2.5$$

A similar behavior is observed for different values of n .

4.4. Maximum flow height

For an observer located at $x > 0$, the maximum height denoted by $h_{max}(x)$ is reached at time $t = t_{max}^*(x)$ (see Figs. 5). Observe that $h_{max}(x) \approx 0.684 H$ for small x , as expected, while $h_{max}(x)$ decreases in $1/x$ for large x , as suggested by the envelope of free surfaces on Fig. 3. This suggests the following scaling law:

$$\frac{h_{max}(x)}{H} \approx 0.684 \frac{L}{L+x} \quad (15)$$

where the coefficients are furnished by a non-linear least-square fitting.

The time when the maximum flow height is reached behaves as x^5 for large x and $x^{1/5}$ for small x . This suggests:

$$t_{max}(x) \approx 2 \left(\frac{x}{L} \right)^{1/5} + 2.1 \left\{ \left(\frac{L+x}{L} \right)^5 - 1 \right\} \quad (16)$$

5. Comparisons with experiments

Some experiments were performed with silicon: the first paragraph presents rheometry while the experimental setup is detailed in the second paragraph. This section ends with the comparison between theory and both experiments for silicon and previous measurements available in the literature for other various materials.

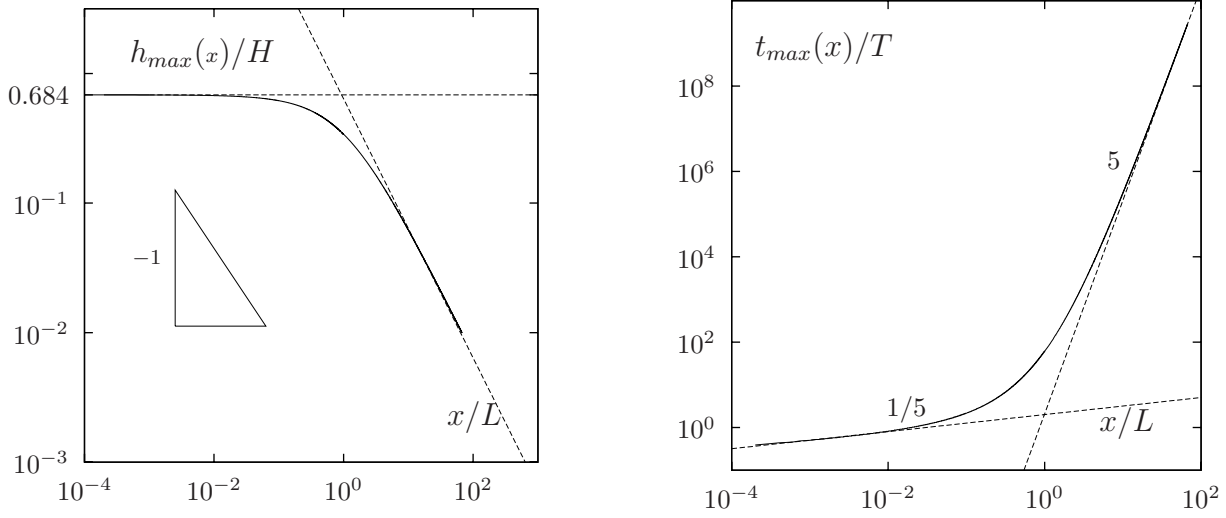


Figure 5. When $n = 1$: (a) maximum flow height $h_{max}(x)$; (b) time of maximum flow height $t_{max}(x)$.

5.1. Material properties and rheometry

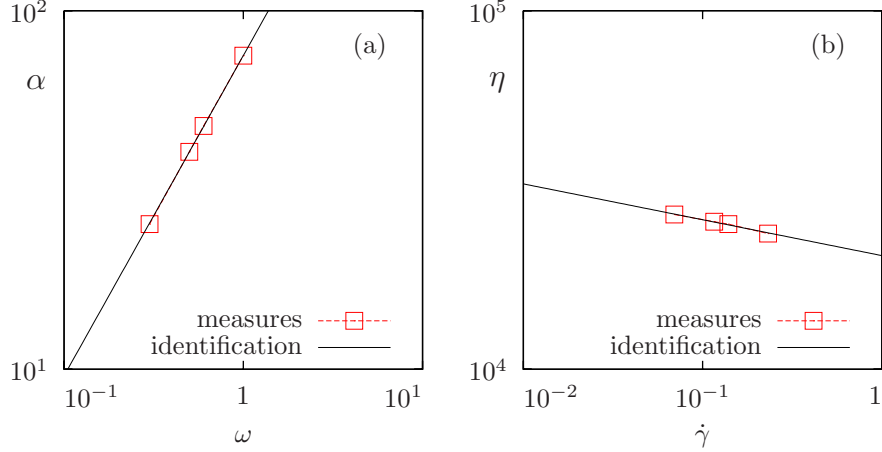


Figure 6. Rheometry on silicone: (a) torque α versus rotation speed ω and determination of the power-law index n ; (b) viscosity η versus the shear rate $\dot{\gamma}$ and determination of the consistency K .

We used a transparent synthetic polymer SGM 36. Made by Dow Corning (USA), SGM 36 is the industrial code of a polymer liquid between 200 and 550 K. It consists of a linear polydimethylsiloxane molecules. The flow curves of was determined using a Brookfield HB DV-I+ rheometer with the spindle #7. The

results are obtained in term of rotation speed ω , torque α , and apparent viscosity η . Then, there are converted into shear rate and shear stress or apparent viscosity. The procedure identify first the power-law index $n = 0.89$ by expressing the torque versus the speed as $\alpha = c\omega^n$ for some constant c (see Fig. 6.a). Next, rounding n to 0.9 and using numerical data from [19], table 1, column 7, we obtain an explicit linear expression between the rotation speed ω and the shear stress $\dot{\gamma}$. Then, in a second step, expressing the apparent viscosity versus the shear rate as $\eta = K\dot{\gamma}^{n-1}$, we identify the consistency $K = 20\,750\text{ Pa}\cdot\text{s}^{n-1}$ (see Fig. 6.b).

The material exhibits also a strong viscoelastic behavior with a relaxation time between 10 and 1 seconds over the range of shear strain rate from 10^{-2} to 1 s^{-1} , respectively [22]. Elastic recovery of strain occurs when it is deformed for times shorter than the relaxation time. In the context of the dam break problem, the time scale is 2 to 3 orders of magnitude larger and viscoelastic effects can be neglected.

5.2. Experimental set-up

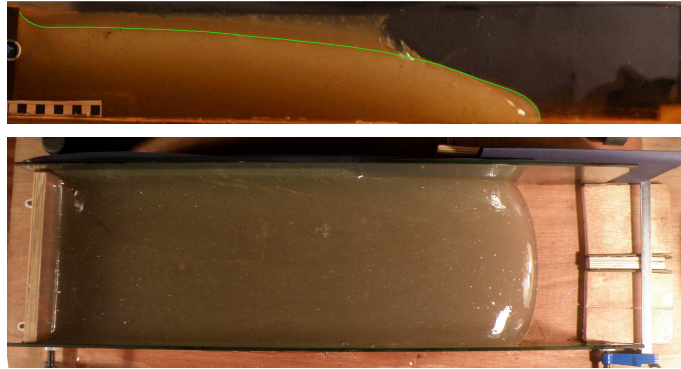


Figure 7. Experimental set-up: (a) face view, where the red line indicates the free surface as generated by image processing; (b) top view.

We used an horizontal channel (see Fig. 7.a) of width W , confined between two plates of Plexiglas, with a reservoir of length L and height H . Fig. 7.b shows that the flow front is relatively flat, suggesting that the slump is largely two-dimensional and the side walls do not have much effect. (see also Fig. 6 in [5] or Fig. 8 in [20] for similar considerations). Slip at the side walls is enforced, thanks to a penetrating grease, while the fluid sticks at the wood bottom boundary. Both widths $W = 115\text{ mm}$ and 225 mm have been tested in order to check that tridimensional effects are negligible and that measurements are independent of the width W . Both reservoir channel $L = 160\text{ mm}$ and 320 mm length have been tested, while $H = 115\text{ mm}$. Digital photography of the front view are performed with a period of 20 seconds. Using an image processing tool, we are able to extract the flow profiles and to obtain the successive front positions x_f .

5.3. Comparisons

For a Newtonian fluid ($n = 1$), the theoretical prediction is compared with two available measurements: on Fig. 8.a with a corn sirup [5, Fig. 7.a] and on Fig. 8.b with a glucose solution [20]. Observe the good concordance between predictions and measurements for both materials. The small time flow regime on Fig. 8.b develops a slope equal to one suggesting a first inertia flow regime. Anyhow, a finer comparison

	$L(cm)$	$H(cm)$	$\rho(g/cm^3)$	n	$K(m.k.s)$
sirup	40	2.2	1.40	1.00	4
glucose	11, 44	5.5	1.40	1.00	12
silicon	16, 40	11.5	1.40	0.90	20 750
gum	40	2.2, 3.2	1.00	0.50	7.5
apple sauce	40	3.6	1.04	0.27	8
kaolin	40	3.7, 4.35	1.50	0.40	34

Table 1
Flow and material parameters used for the comparisons.

with the corresponding Ritter solution $x_f = (gH)^{\frac{1}{2}}t$ is not satisfactory and better explained by the lifting of the dam in [20]. The complete set of flow and material parameters used for all the comparison in this paragraph are summarized in table 1.

For a non-Newtonian power-law fluid ($n \neq 1$), the theoretical predictions are compared with several measurements associated to different values of the power index n . Fig. 8.c shows the comparisons with our present measurements on silicon with $n = 0.9$. Fig. 8.d presents measurements on a xantham gum [5, Fig 9.b] with $n = 0.5$. Observe also the small time flow regime: as for glucose, this first regime is not related to inertia effects and could be due to the lifting of the dam. Fig. 9.a presents a comparable situation with apple sauce [5, Fig 12], with $n = 0.27$. Finally, Fig. 9.b shows a comparison with kaolin [5, Fig 11] with $n = 0.4$. Observe that for largest times, the fluid stops. Kaolin is usually represented by the Herschel-Bulkley power-law yield stress model and associated shallow water approximation are able to predict this behavior [18,4] This feature will be integrated in our numerical simulation in the future.

Let us come back to the present measurements on silicon: Fig. 10 shows the free surface profiles for the two reservoir lengths with the same height $H = 11.5$ cm and width $W = 22.5$ cm. The profiles are globally in good concordance with some small discrepancies: the theory predicts a lower profile at upstream and a higher one at downstream. A possible explanation of this discrepancies could be the development of localized viscoelastic effects in the front region, where shear rates are higher.

6. Conclusion

Using silicon, new measurements in the non-Newtonian power-law case has been performed in this paper for the horizontal dam break problem. Based on a new time-space second-order adaptive algorithm, the shallow approximation of the problem has been solved and solutions compared with both silicon and other measurements for Newtonian and non-Newtonian materials. These comparisons confirm the validity of the slow flow shallow approximation equations for the horizontal dam break problem for these materials.

Future works will focus on some improvements of the model by introducing yield stress and inertia terms. The yield stress term is associated to the prediction of an asymptotical arrested state for large times while the inertia term is related to the first flow regime at small times. Also the adaptive numerical algorithm is a good candidate to handle three-dimensional free surface flows: using an asymptotic analysis, these flows are reduced to a shallow flow on a surface with a complex topography. This second improvement will be considered for practical applications for geophysical flows such as mud or volcanic lava flows.

References

- [1] R. A. Adams and J. J. F. Fournier. *Sobolev spaces*. Elsevier, second edition, 2003.
- [2] C. Ancey. *Snow avalanches*, pages 319–338. Springer, 2001.
- [3] C. Ancey. Plasticity and geophysical flows: a review. *J. Non-Newtonian Fluid Mech.*, 142:4–35, 2007.
- [4] N. J. Balmforth and R. V. Craster. A consistent thin-layer theory for Bingham plastics. *J. Non-Newtonian Fluid Mech.*, 84(1):65–81, 1999.
- [5] N. J. Balmforth, R. V. Craster, P. Perona, A. C. Rust, and R. Sassi. Viscoplastic dam breaks and the Bostwick consistometer. *J. Non-Newtonian Fluid Mech.*, 142(1–3):63–78, 2007.
- [6] N. J. Balmforth, R. V. Craster, A. C. Rust, and R. Sassi. Viscoplastic flow over an inclined surface. *J. Non-Newtonian Fluid Mech.*, 139:103–127, 2006.
- [7] A. J. C. Barré de Saint-Venant. Théorie et équations générales du mouvement non permanent des eaux courantes. *Comptes Rendus des séances de l'Académie des Sciences, Paris, France, Séance 17*, 73:147–154, 1871.
- [8] E. C. Bingham. *Fluidity and plasticity*. Mc Graw-Hill, 1922.
- [9] P. Coussot. Steady, laminar, flow of concentrated mud suspensions in open channel. *J. Hydr. Res.*, 32(4):535–559, 1994.
- [10] M. Fortin and R. Glowinski. *Augmented Lagrangian methods*. Elsevier, 1983.
- [11] J.-F. Gerbeau and B. Perthame. Derivation of viscous Saint-Venant system for laminar shallow water; numerical validation. *Discrete and continuous dynamical systems - serie B*, 1(1):89–102, 2001.
- [12] R. W. Griffiths. The dynamics of lava flows. *Annual Review of Fluid Mechanics*, 32:477–518, 2000.
- [13] M. A. Hampton, H. J. Lee, and J. Locat. Submarine landslides. *Reviews of geophysics*, 34(1):33–59, 1996.
- [14] W. H. Herschel and T. Bulkley. Measurement of consistency as applied to rubber-benzene solutions. *Am. Soc. Test Proc.*, 26(2):621–633, 1926.
- [15] H. E. Hupper. The propagation of two-dimensional and axisymmetric viscous gravity currents over a rigid horizontal surface. *J. Fluid Mech.*, 121:43–58, 1982.
- [16] D. Laigle and P. Coussot. Numerical modeling of mudflows. *J. Hydr. Engrg.*, 123(7):617–623, 1997.
- [17] K. F. Liu and C. C. Mei. Approximate equations for the slow spreading of a thin sheet of a Bingham plastic fluid. *Phys. Fluids A*, 2:30–36, 1990.
- [18] G. P. Matson and A. J. Hogg. Two-dimensional dam break flows of Herschel-Bulkley fluids: The approach to the arrested state. *J. Non-Newtonian Fluid Mech.*, 142:79–94, 2007.
- [19] P. Mitschka. Simple conversion of Brookfield R.V.T. readings into viscosity functions. *Rheol. Acta*, 21:207–209, 1982.
- [20] J.-M. Piau and K. Debiane. Consistometers rheometry of power-law viscous fluids. *J. Non-Newtonian Fluid Mech.*, 127:213–224, 2005.
- [21] P. Saramito, N. Roquet, and J. Étienne. RHEOLEF: A finite element environment, i.e. some C++ classes and unix commands. <http://www-lmc.imag.fr/lmc-edp/Pierre.Saramito/rheolef>, 2009.
- [22] R. Weijermars. Finite strain of laminar flows can be visualized in SGM36-polymer. *Naturwissenschaften*, 73(1):33–34, 1986.

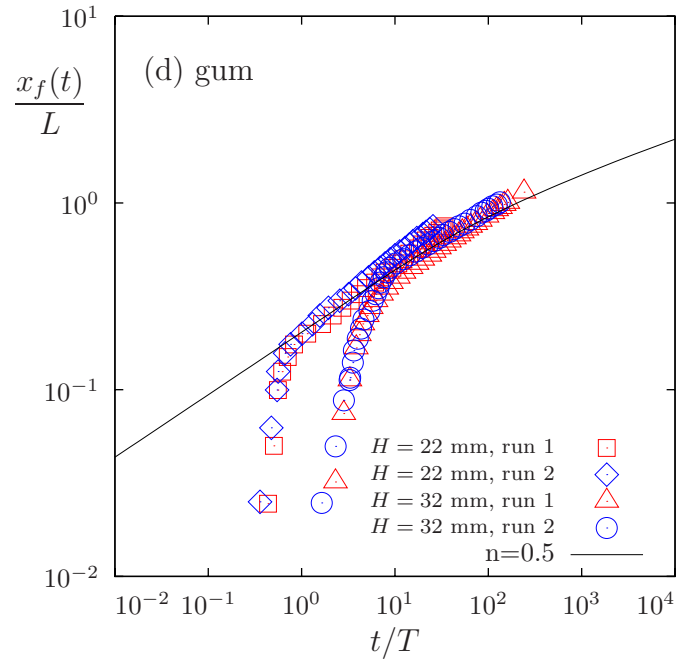
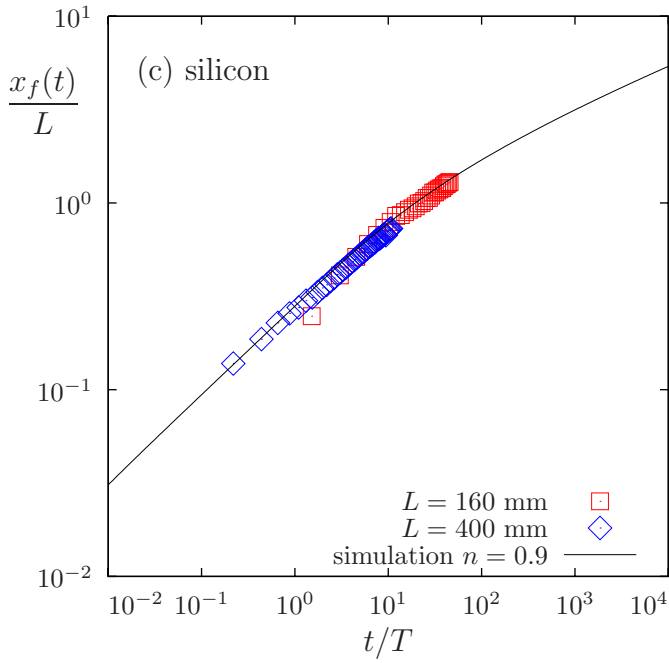
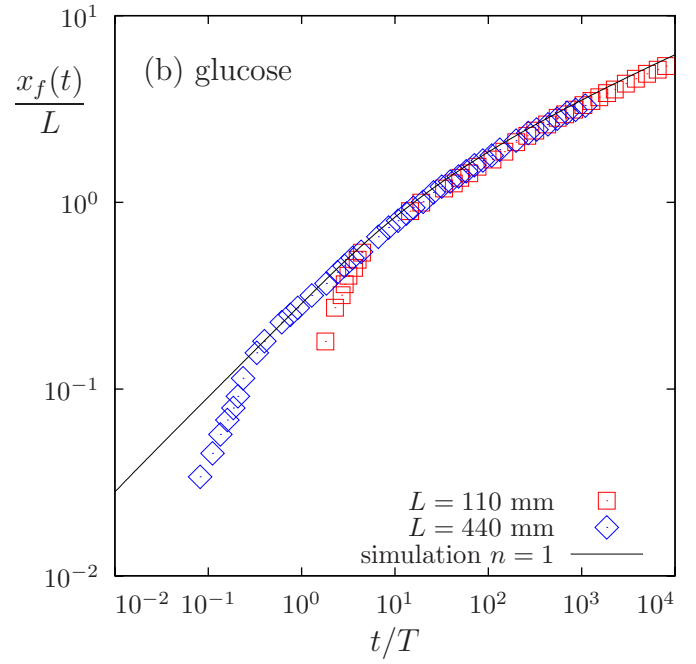
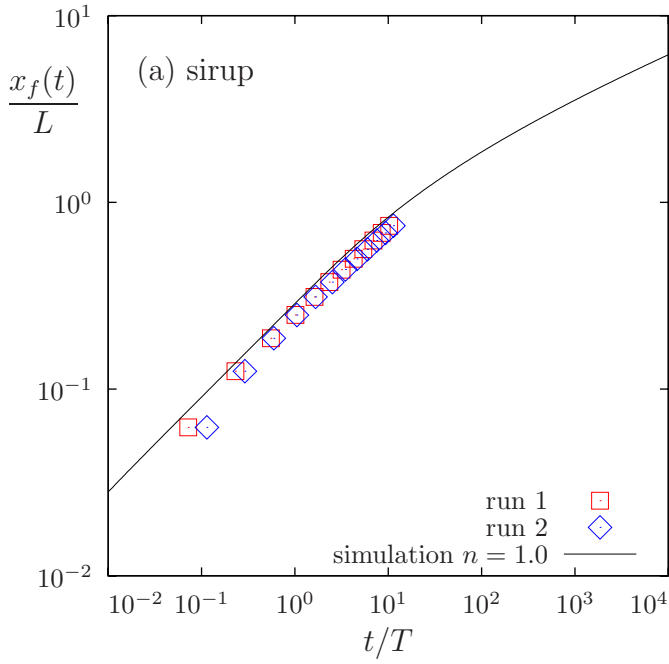


Figure 8. Front position: comparison between experimental measurements and theoretical predictions with (a) corn sirup [5, Fig 7.a] ; (b) glucose [20] ; (c) silicon ; (d) gum [5, Fig 9.b].

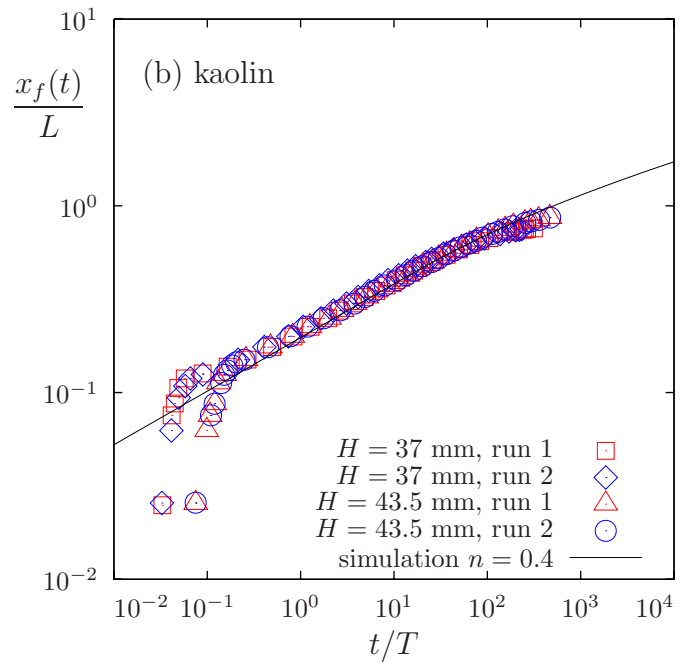
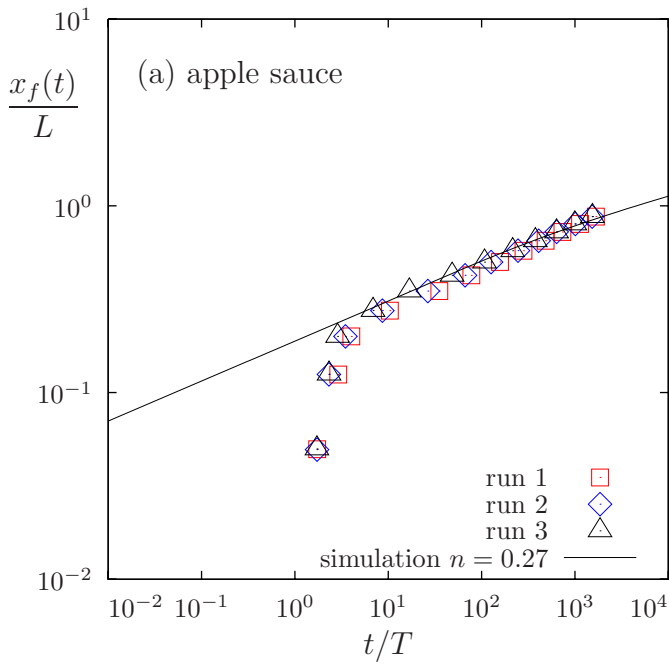


Figure 9. Front position: comparison between experimental measurements and theoretical predictions with (a) apple sauce [5, Fig 12] ; (b) kaolin [5, Fig 11].

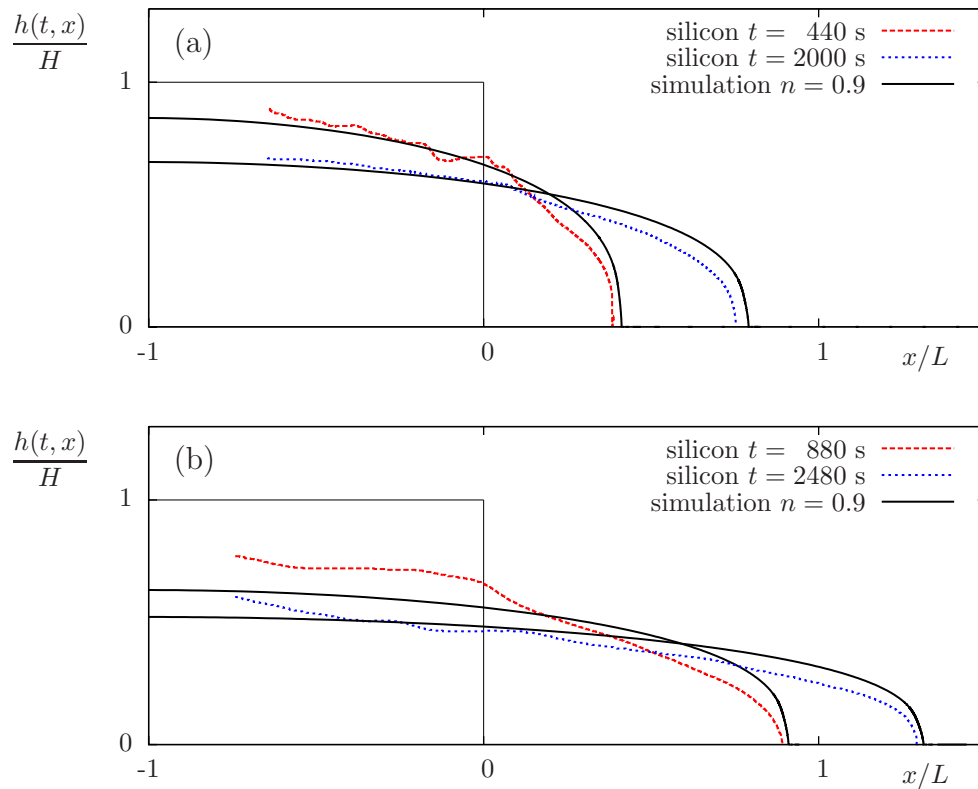


Figure 10. Free surface : comparison between theoretical prediction with $n = 0.9$ and experimental measurements with silicon when $H = 115\text{ mm}$ and $W = 225\text{ mm}$: (a) $L = 440\text{ mm}$, and (b) $L = 160\text{ mm}$.

Appendix A. Numerical resolution

This section focuses on time and space approximations of the reduced problem. A semi-implicit time approximation scheme is first presented, and improved by a fixed-point internal loop. Each step requires the resolution of a linear second-order elliptic sub-problem.

A.1. Time approximation and algorithms

Since the initial condition $h_0(x)$ is discontinuous, the solution of the parabolic problem is singular at the vicinity of $t = 0$. For that reason, we opt for a second order fully implicit and variable time step algorithm. The time step are chosen small at the vicinity of $t = 0$ and increases with a geometric progression. Let $(t_m)_{m \geq 0}$ denotes the time discretization sequence and $\Delta t_m = t_{m+1} - t_m$, $m \geq 0$ be the time step. The first-order time derivative is approximated by the following second-order finite difference scheme, defined for all function $\varphi \in C^0$ by:

$$\begin{aligned} \frac{\partial \varphi}{\partial t}(t_{m+1}) &= \frac{2\Delta t_m + \Delta t_{m-1}}{\Delta t_m(\Delta t_m + \Delta t_{m-1})} \varphi(t_{m+1}) - \frac{\Delta t_m + \Delta t_{m-1}}{\Delta t_m \Delta t_{m-1}} \varphi(t_m) \\ &\quad + \frac{\Delta t_m}{(\Delta t_m + \Delta t_{m-1})\Delta t_{m-1}} \varphi(t_{m-1}) + \mathcal{O}(\Delta t_m^2 + \Delta t_{m-1}^2) \end{aligned}$$

Let us introduce $(\hat{h}^m)_{m \geq 0}$, $\hat{h}^m(\hat{x}) \approx \hat{h}(m\Delta \hat{t}, \hat{x})$, defined recursively by the following algorithm:

ALGORITHM 1

- $m = -1, 0$: $\hat{h}^0 := \hat{h}^{-1} := \hat{h}(t = 0)$
- $m \geq 1$: given \hat{h}^{m-1} and \hat{h}^m , find \hat{h}^{m+1} such that:

$$\frac{2\Delta t_m + \Delta t_{m-1}}{\Delta t_m(\Delta t_m + \Delta t_{m-1})} \hat{h}^{m+1} - \frac{d}{d\hat{x}} \left(\nu_n \left(\hat{h}^{m+1}, \frac{d\hat{h}^{m+1}}{d\hat{x}} \right) \frac{d\hat{h}^{m+1}}{d\hat{x}} \right) \quad (\text{A.1})$$

$$= \frac{\Delta t_m + \Delta t_{m-1}}{\Delta t_m \Delta t_{m-1}} \hat{h}^m - \frac{\Delta t_m}{(\Delta t_m + \Delta t_{m-1})\Delta t_{m-1}} \hat{h}^{m-1} \quad \text{in }]-1, +\infty[\quad (\text{A.2})$$

$$\frac{d\hat{h}^{m+1}}{d\hat{x}}(-1) = \frac{d\hat{h}^{m+1}}{d\hat{x}}(+\infty) = 0 \quad (\text{A.3})$$

where, for all $\xi \geq 0$ and $\zeta \in \mathbb{R}$:

$$\nu_n(\xi, \zeta) = \begin{cases} 0, & \text{when } \zeta = 0, \\ \frac{n}{2n+1} \xi^{2+\frac{1}{n}} |\zeta|^{-1+\frac{1}{n}} \text{sgn}(\zeta), & \text{otherwise} \end{cases}$$

Algorithm 1 corresponds to an implicit second-order backward discretization scheme with variable time step. This scheme is used for all the computations which are undertaken in the next sections. The initial time-dependent problem is transformed to a sequence of nonlinear sub-problems (A.2)-(A.3), since, at each iteration m , \hat{h}^{m+1} is unknown. The simplest idea is to solve each sub-problem by using an inner fixed-point loop:

ALGORITHM 2.a

- $k = 0$: $\varphi^0 := \hat{h}^m$

- $k \geq 1$: given φ^k , find φ^{k+1} such that:

$$\alpha_m \varphi^{k+1} - \frac{d}{d\hat{x}} \left(\nu_n \left(\varphi^k, \frac{d\varphi^k}{d\hat{x}} \right) \frac{d\varphi^{k+1}}{d\hat{x}} \right) = f_m \quad \text{in }]-1, +\infty[$$

$$\frac{d\varphi^{k+1}}{d\hat{x}}(-1) = \frac{d\varphi^{k+1}}{d\hat{x}}(+\infty) = 0$$

where

$$\alpha_m = \frac{2\Delta t_m + \Delta t_{m-1}}{\Delta t_m(\Delta t_m + \Delta t_{m-1})}$$

$$f_m = \frac{\Delta t_m + \Delta t_{m-1}}{\Delta t_m \Delta t_{m-1}} \hat{h}^m - \frac{\Delta t_m}{(\Delta t_m + \Delta t_{m-1})\Delta t_{m-1}} \hat{h}^{m-1}$$

This inner loop stops when the residual term is less than a given tolerance $\varepsilon > 0$. Then, we set $\hat{h}^{m+1} := \varphi^k$. Algorithm 2.a reduces to an elliptic second order differential equation with non-constant coefficients.

In practice, we observe that this algorithm converges only for $n \in]1/2, 2[$ and has poor convergence properties for large meshes. So, in order to solve the nonlinear sub-problem (A.2)-(A.3), we define a more robust algorithm:

ALGORITHM 2.b

- $k = 0$: $\varphi^0 := \hat{h}^m$
- $k \geq 1$: given φ^k , find φ^{k+1} such that:

$$\alpha_m \varphi^{k+1} - \frac{d}{d\hat{x}} \left(\mu_n(\varphi^k) \left| \frac{d\varphi^{k+1}}{d\hat{x}} \right|^{\frac{1}{n}} \right) = f_m \quad \text{in }]-1, +\infty[$$

$$\frac{d\varphi^{k+1}}{d\hat{x}}(-1) = \frac{d\varphi^{k+1}}{d\hat{x}}(+\infty) = 0$$

where, for all $\xi \geq 0$:

$$\mu_n(\xi) = \frac{n}{2n+1} \xi^{2+\frac{1}{n}}$$

For a fixed iteration $k \geq 0$, observe that the sub-problem (A.4)-(A.4) is still nonlinear: this is the so-called p -laplacian problem, with $p = 1 + 1/n > 1$. Let $L^p(-1, +\infty)$ and $W^{1,p}(-1, +\infty)$ denote the usual Sobolev functional spaces [1]. Observe that the solution of (A.4)-(A.4) is characterized as the minimum of the following energy-like function, defined for all $\varphi \in W^{1,p}(-1, +\infty)$ by:

$$J_{k,m}(h) = \frac{\alpha_m}{2} \int_{-1}^{+\infty} \varphi^2 dx + \frac{n}{n+1} \int_{-1}^{+\infty} \mu_n(\varphi_k) |\varphi'|^{1+\frac{1}{n}} dx - \int_{-1}^{+\infty} f_m \hat{h} dx$$

Following [10, p. 128], let us consider the quantity $\delta = \varphi' \in L^p(-1, +\infty)$ as an independent variable. The constraint $\delta - \varphi' = 0$ is enforced by using a Lagrange multiplier $\tau \in L^{p'}(-1, +\infty)$, where $p' = 1 - 1/p = 1/(1+n)$. The following augmented Lagrangian is then introduced:

$$L_{k,m}((\varphi, \delta); \tau) = \frac{\alpha_m}{2} \int_{-1}^{x_e} \varphi^2 dx + \frac{n}{n+1} \int_{-1}^{x_e} \mu_n(\varphi_k) |\delta|^{1+\frac{1}{n}} dx - \int_{-1}^{x_e} f_m \varphi dx + \int_{-1}^{x_e} (\varphi' - \delta) \tau dx + \frac{\beta}{2} \int_{-1}^{x_e} |\varphi' - \delta|^2 dx$$

where $\beta > 0$ is the augmentation parameter of the Lagrangian. The previous minimization problem is equivalent to the following saddle point problem

$$\inf_{(\varphi, \delta) \in W^{1,p} \times L^p} \sup_{\tau \in L^{p'}} L_{k,m}((\varphi, \delta); \tau)$$

Notice that the solution is independent of β since the solution of the saddle point problem satisfies $\delta = \varphi'$. An Uzawa minimization algorithm for finding the saddle point of $L_{m,k}$ writes:

ALGORITHM 3

- $l = 0$: let δ_0 and τ_0 arbitrarily chosen.
- $l \geq 0$: let δ_l and τ_l being known, find φ_{l+1} such that

$$\begin{aligned} \alpha\varphi_{l+1} - \beta\varphi_{l+1}'' &= f - (\tau_l - \beta\delta_l) \quad \text{in }]-1, x_e[\\ \varphi_{l+1}'(-1) &= \varphi_{l+1}'(+\infty) = 0 \end{aligned} \quad (\text{A.4})$$

then, compute δ_{l+1} in a point-by-point way:

$$\delta_{l+1}(x) = \Phi_{n,\beta}(\mu_n(\varphi_k(x)), \tau_l(x) + \beta\varphi_{l+1}'(x)) \quad (\text{A.5})$$

and finally, compute explicitly τ_{l+1} as:

$$\tau_{l+1} = \tau_l + \beta(\varphi_{l+1}' - \delta_{l+1}) \quad (\text{A.6})$$

Problem (A.4) is linear and completely standard: it can be very efficiently solved, especially in one space dimension. The nonlinearity is treated in (A.5) where the function $\Phi_{n,\beta}$ has been introduced: it is defined for all $\bar{\mu}, \zeta \in \mathbb{R}$ by:

$$\Phi_{n,\beta}(\bar{\mu}, \zeta) = \arg \min_{\delta \in \mathbb{R}} \frac{\bar{\mu}n}{n+1} |\delta|^{1+\frac{1}{n}} + \frac{\beta}{2} \delta^2 - \zeta \delta$$

Since this minimization problem in \mathbb{R} is convex, its solution $\delta \in \mathbb{R}$ is unique and then $\Phi_{n,\beta}$ is well defined. The minimization problem is also differentiable and its solution satisfies $\bar{\mu}|\delta|^{\frac{1}{n}} \text{sgn}(\delta) + \beta\delta - \zeta = 0$ where sgn denotes the sign function. Notice that when $n = 1$, i.e. the Bingham model, the computation is explicit: $\delta = \zeta/(\bar{\mu} + \beta)$. In the general case of the Hershel-Bulkley model, when $n > 0$, we consider the Newton algorithm:

- $q = 0$: let δ_0 given.
- $q \geq 0$: let δ_q being known and compute

$$\delta_{q+1} = \delta_q - \frac{\bar{\mu}|\delta_q|^{\frac{1}{n}} \text{sgn}(\delta_q) + \beta\delta_q - \zeta}{\frac{1}{n}\bar{\mu}|\delta_q|^{\frac{1}{n}-1} + \beta}$$

In practice, the Newton algorithm is initialized with $\delta_0 = \zeta/(\bar{\mu} + \beta)$ and we observe that the convergence is very fast. Also, algorithms 2.b and 3 are combined in a flatten algorithm, where only one iteration of the l inner loop is performed. This leads to an efficient and robust strategy for the numerical resolution of the nonlinear problem.

A.2. Space approximation and adaptive subdivision

The problem is discretized with respect to the space variable \hat{x} by a quadratic finite element method in a bounded interval $]-1, \hat{x}_e[$, where \hat{x}_e is chosen sufficiently large. The matrix of the subproblems involves a bandwidth equal to five: the linear system can be efficiently solved by using a direct method. The numerical implementation bases on the finite element library [21].

At each time step, we used a mesh adaptive procedure that bases on a criterion χ related to the flow rate plus a time derivative term:

$$\chi(\hat{t}, \hat{x}) = \left(\nu_n \left(\hat{h}, \frac{\partial \hat{h}}{\partial \hat{x}} \right) \left(\frac{\partial \hat{h}}{\partial \hat{x}} \right)^2 + \left(\frac{\partial \hat{h}}{\partial \hat{t}} \right)^2 \right)^{1/2}$$

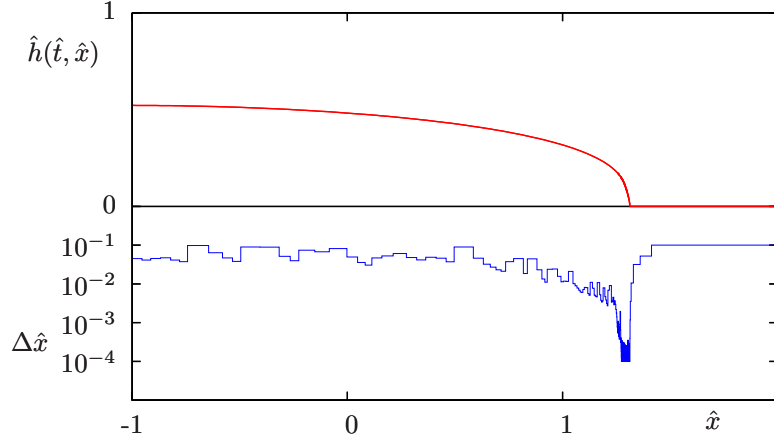


Figure A.1. Adaptive subdivision for the dam break problem $n = 0.9$, $t = 15$: 1145 elements.

The time derivative term is approximated by the previous second order scheme. The time step is locally optimized for minimizing the local interpolation error χ :

$$\Delta\hat{x}(\hat{t}, \hat{x}) = \min \left(\Delta\hat{x}_{\min}^{-2}, \max \left(\Delta\hat{x}_{\max}^{-2}, \left| \frac{\partial^2 \chi}{\partial \hat{x}^2} \right| \right) \right)$$

where $\Delta\hat{x}_{\min} = 10^{-4}$ and $\Delta\hat{x}_{\max} = 10^{-1}$. At time t_m , a subdivision is then automatically generated as $\hat{x}_{i+1} = \hat{x}_i + \Delta\hat{x}(\hat{t}_m, \hat{x}_i)$, $i \geq 0$, and $\hat{x}_0 = -1$. As shown on Fig. A.1, this procedure is capable of capturing the front position, where gradients are locally important and the solution becomes singular: the discretization step tends to $\Delta\hat{x}_{\min}$. Conversely, at downstream, after the front, the solution is zero and the discretization step is $\Delta\hat{x}_{\max}$.